

Chapter

Modeling Aerosol-Cloud-Precipitation Interactions in Mountainous Regions: Challenges in the Representation of Indirect Microphysical Effects with Impacts at Subregional Scales

*Ana P. Barros, Prabhakar Shrestha, Steven Chavez
and Yajuan Duan*

Abstract

In mountainous regions, the nonlinear thermodynamics of orographic land-atmosphere interactions (LATMI) in organizing and maintaining moisture convergence patterns on the one hand, and aerosol-cloud-precipitation interactions (ACPI) in modulating the vertical structure of precipitation and space-time variability of surface precipitation on the other, are difficult to separate unambiguously because the physiochemical characteristics of aerosols themselves exhibit large sub-regional scale variability. In this chapter, ACPI in the Central Himalayas are examined in detail using aerosol observations during JAMEX09 (Joint Aerosol Monsoon Campaign 2009) to specify CCN activation properties for simulations of a premonsoon convective storm using the Weather Research and Forecasting (WRF) version 3.8.1. The focus is on contrasting AIE during episodes of remote pollution run-up from the Indo-Gangetic Plains and when only local aerosols are present in Central Nepal. This study suggests strong coupling between the vertical structure of convection in complex terrain that governs the time-scales and spatial organization of cloud development, CCN activation rates, and cold microphysics (e.g. graupel production is favored by slower activation spectra) that result in large shifts in the spatial distribution of precipitation, precipitation intensity and storm arrival time.

Keywords: aerosol-cloud-precipitation interactions, ACPI, orography, indirect effect, Himalayas

1. Introduction

The aerosol indirect effect (AIE) refers to the cascade of processes (aerosol-cloud-precipitation interactions, ACPI) linking the space-time variability of aerosol physiochemical properties to modification of the vertical structure of precipitation microphysics that result in changes in timing and spatial patterns of precipitation

accumulation at the ground. In mountainous regions, orographic modification of atmospheric circulations at multiple scales can further modulate ACPI and consequently have a significant impact on the spatial distribution of precipitation, that is to say the allocation of freshwater input and hydrologic response among adjacent mountain catchments [1–3].

The climatology of the observed strong peak of aerosol optical depth in the premonsoon season in the Indo Gangetic Plains (IGP) has been well documented in numerous studies using satellite retrievals [4–7]. At regional and continental scales, [8] points out that, in the South Asian monsoon region such as the Indian Subcontinent and Himalayas, the net effect of ACPI before and during the monsoon depends on large-scale circulations, moisture availability, and the presence of aerosol hot-spots. Reduction of the efficiency of raindrop dynamics (coalescence and breakup) on account of the presence of very high concentrations of small cloud droplets where aerosol concentrations are very high (aerosol hot-spots) results in delay of precipitation at the surface while very small cloud droplets are transported to higher levels in the troposphere in the direction of storm propagation. Upward transport results in a large population of supercooled drops aloft that freeze, interact with each other to form graupel and hail and subsequently melt as they fall, thus invigorating deep convection through release and production of latent heating at different levels in the troposphere. Higher CCN concentrations from fine aerosol particles slow the conversion of cloud drops into raindrops, thus suppressing rainfall production initially followed by intensification later [9]. Besides the time-delay of precipitation processes, several studies [10–19] have shown that the aerosol effect on cloud microphysical processes strongly depends on specific environmental conditions, varies with cloud types, and thus storm regime. Overall, these studies suggest that mechanisms of aerosol-cloud-rainfall interactions are very complex and highly nonlinear, and therefore transferability and generalization of the results learned from one case study for a particular storm may not be applicable for other storm in different environmental conditions, including climate regime and topography. The latter plays a significant role in airflow modification which in turn strongly impact microphysical pathways. At subregional scales, given similar regional meteorology, these dynamic feedbacks translate into smaller areas of enhanced convective precipitation that is a redistribution of precipitation conditional on aerosol-cloud interactions. Intercomparison modeling studies using CN with different activation characteristics suggest that the timing and intensity of precipitation are tightly linked to regional and subregional scale aerosol characteristics. Recent NWP (Numerical Weather Prediction) simulations in the Southern Appalachians Mountains (complex terrain with moderate elevation <2500 m) show that using regional CCN activation characteristics obtained from field measurements [20] has strong impact on rainfall structure as compared to standard continental aerosol by reducing unrealistic light rainfall on the one hand, and by intensifying convection on the other due to strong modification of cloud microphysics, even more so in the case of local vis-a-vis synoptic forcing [21, 22]. This begs the question of whether the characterization of regional aerosol is not only desirable, but indeed necessary toward achieving a substantial improvement in NWP's predictive skill at high spatial resolution and short time-scales (< 24 hr) toward decreasing phase errors in storm arrival and improving rainfall intensity [2, 23, 24].

Shrestha and Barros [7] identified the central region of the Himalayas and adjacent foothills as a region of potentially high ACPI as the synoptic scale aerosol plume in the IGP penetrates, runs up and accumulates along deep river valleys. Indeed, [25] showed how IGP aerosol can remain sequestered to form pools over low lying areas and valleys in the Middle Himalaya after there is a full retreat of the pollution over the IGP. The aerosol pool is eventually scavenged by the formation of low-level clouds and fog, and washed out by rainfall similar to subregional scale forcing in

the inner region of the Southern Appalachians investigated by [21, 22]. Specifically, [26] showed that, in the presence of regional scale aerosol clouds and during dry periods, the mean volume aerosol concentration increased, and so did the aerosol mass concentrations in two different valleys of Central Nepal, the Marshyangdi and the Kathmandu, followed by rain-out. In addition, the topography of the region was found to play an important role in modulating the diurnal cycle of aerosol number concentration due to the diurnal cycle of katabatic and anabatic winds. Previous studies by [27–30] over the central Himalayas in Nepal have shown that the space-time distribution of rainfall and the terrain are strongly intertwined in the region. Depending upon the type of cloud systems and synoptic conditions, changes in aerosol number concentration and chemical properties influence the microphysical pathways of ACPI in different ways, resulting in suppression of rainfall, storm invigoration, and even spatial displacement of rainfall [10, 13, 31–35]. The particle sizes measured during the Joint Aerosol Monsoon Experiment (JAMEX09) in Central Nepal indicate that the dominant aerosol mode is around 100 nm [26], which is also consistent with the predominance of fine aerosol (< 350 nm) found by [36] in the Himalayan foothills using MISR (Multi Imaging Spectro-Radiometer) observations.

The dependence of the aerosol sensitivity on environmental conditions and storm regimes necessitates a better understanding of the joint climatology of aerosol characteristics, regional storm systems and associated precipitation (e.g., premonsoon, monsoon, post-monsoon and winter precipitation in the Himalayas). In-situ measurement of aerosol chemical and physical properties for the different seasons of the year is required to evaluate the sensitivity of the aerosol for different storm regimes using numerical models. Only then, a clear picture of ACPI might emerge. Here, we present an exploratory study to investigate the CCN sensitivity of the numerical simulation of a premonsoon season storm in the Central Himalayas associated with the intrusion of a major IGP aerosol plume (**Figure 1**). The CCN spectra used in the study were estimated from the in-situ measured aerosol size distribution and chemical composition during the Joint Aerosol Monsoon Experiment 2009 (JAMEX09) [26, 37].

The ultimate objective is to investigate ACPI for remote aerosol linked to run-up of a major haze event over the IGP against locally produced aerosol that exhibit very different activation behavior (hygroscopicity) even when concentration numbers are not significantly different [26, 37]. Because this study consists of simulations of the same storm system using different CCN, it allows us also to assess quantitatively the likely impact of changes in storm dynamics on precipitation fields at the ridge-valley scale in the Middle Himalaya caused by IGP pollution. Significant shifts in the maxima of the event cumulative precipitation were first observed between the simulations conducted with control continental aerosol spectra in WRF and from JAMEX09 by [38]. Differences in the simulated vertical profile of temperature, water vapor mixing ratio and hydrometeor distributions (indicative of differences in latent heat absorption/release) lead to changes in local circulations, which in turn are tied to landform. In particular, this study suggests strong coupling among CCN activation spectra, the vertical structure of convection in complex terrain, and cold microphysics (e.g., graupel formation) that strongly impacts the spatial distribution of precipitation at the surface. Finally, we discuss the results in the context of regional hydrometeorology and impact on spatial patterns of precipitation accumulation that result from changes in space-time storm evolution displacing convective cells among adjacent catchments in Central Nepal including the Kulekhani Water Reserve (KWR) hydropower dam, which provides critical electricity to Kathmandu, and the Indrawati basin (IDR), the headwaters of the Sun Koshi river that links central to eastern Nepal (**Figure 2**). The chapter is structured as follows: Section 2 describes the experimental setup for the simulation. Results are discussed in Section 3. Summary and conclusions are presented in Section 4.

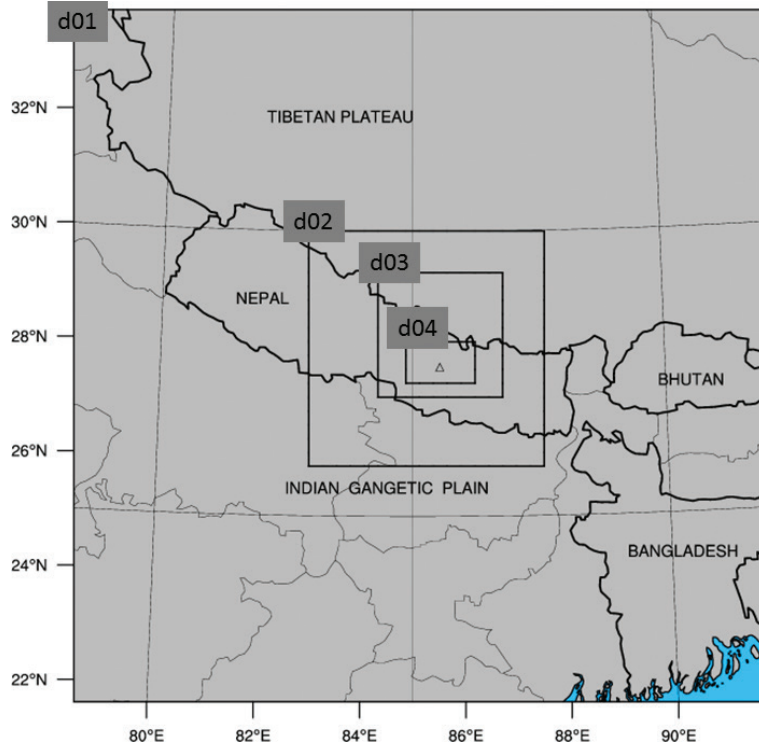


Figure 1.

Map of the region of study. The four nested domains used for WRF model simulations are centered over Central Nepal. Domain d01 (27 km) encompass the Indian Gangetic plain (IGP) and the Tibetan plateau extending up to Bhutan and Bangladesh in the east. Domains d02 (9 km) and d03 (3 km) are over Central Nepal. Domain d04 (1 km) encloses the Kathmandu Valley (marked with triangle).

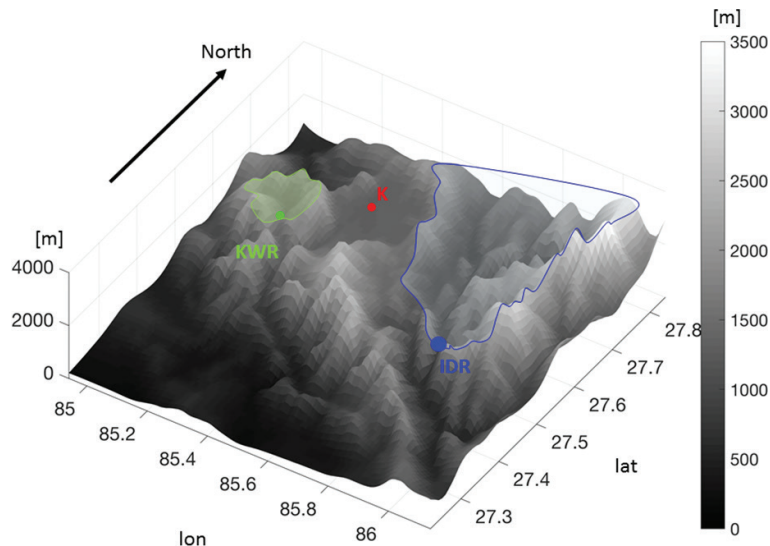


Figure 2.

Topography of Central Nepal (d04). The city of Kathmandu is identified by the letter K, in red. The catchment contributing to the Kulekhani dam (green, KWR), and the southern part of the Indrawati basin (blue, IDR) within d04 are marked and delineated.

2. Numerical experiments of ACPI sensitivity to CCN

2.1 WRF model setup

The Advanced Weather Research and Forecasting (WRF) model Version 3.8.1 [39] was used for numerical simulations of a northwesterly convective storm over Central Nepal on May 15–16, 2009 during JAMEX09. The model configuration was set up similar to [3] with four one-way nested domains with horizontal grid spacing of 27-, 9-, 3-, and 1-km, corresponding to grid sizes of 51×51 , 52×52 , 73×73 , and 121×73 for the first (d01), second (d02), third (d03), and fourth (d04) domains, respectively (**Figure 1**). In order to resolve low-level cloud formation and precipitation processes, a terrain-following vertical grid with 90 layers was constructed with 30 levels in the lowest 1 km AGL and the model top at 50 hPa. WRF simulations during a two-day period were conducted starting at 00:00 UTC 14 May 2009 (5:45 LT in Nepal) and ending at 00:00 UTC May 16, 2009. The first six hours of simulation were disregarded for analysis.

Initialization and lateral boundary conditions are updated every 6-hours and interpolated in-between using the National Centers for Environmental Prediction (NCEP) Final Operational Global Analysis (FNL) with $1 \times 1^\circ$ horizontal resolution. The Kain-Fritsch cumulus parameterization scheme [40] is used in the first and second domains (27 and 9 km resolution), and convection is resolved explicitly in the third (3 km) and fourth (1 km) domains. Other physics options include Milbrandt and Yau's 2005 (MY05) double moment microphysics [41], a new version of the Rapid Radiative Transfer Model radiation scheme for longwave and shortwave [42], and the unified Noah land-surface model [43] applied for all four domains. Following [2, 3], the Mellor-Yamada-Nakanishi-Niino (MYNN) planetary boundary layer scheme [44] is selected along with the Monin-Obukhov (Janjic Eta) surface layer scheme to better capture low level cloud formation. The soil temperature and moisture fields are also initialized from the NCEP FNL data.

2.2 Modeling experiments with Milbrandt-Yau microphysics

The MY05 double moment microphysics scheme (total number concentration and mixing ratio) is used here to investigate the effects of aerosol properties on the sensitivity of ACPI. Number concentrations of nucleated cloud droplets (N_{CCN}) in MY05 are calculated based on a four-parameter CCN activation spectrum proposed by [45], hereafter referred to as CPB98. This CCN activation scheme has demonstrated improved estimation of cloud droplet numbers as it accounts for the depletion of small-sized condensation nuclei (CN) with increasing supersaturation:

$$N_{CCN}(S_{v,w_{max}}) = CS_{v,w_{max}}^k F\left(\mu, \frac{k}{2}, \frac{k}{2} + 1; -\beta S_{v,w_{max}}^k\right) \quad (1)$$

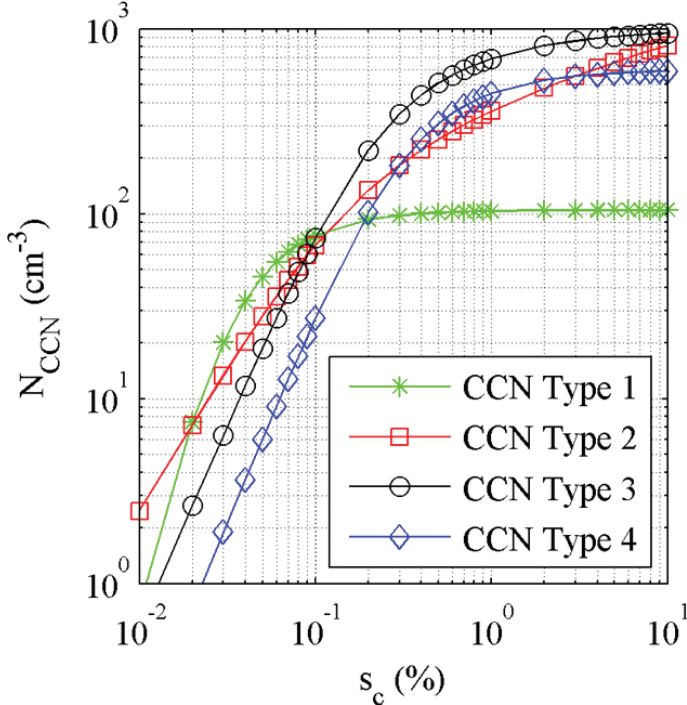
Where $S_{v,w_{max}}$ is the maximum water vapor supersaturation and $F(a, b, c; x)$ is a hypergeometric function. The four fitted parameters in Eq. (1) can be interpreted as follows: C is a scaling factor, k is the slope of the linear relationship between $\log N_{CCN}$ and $\log S_v$, and β indicates the location of the slope break between the fast (linear) CCN activation regime governed by k at lower supersaturation and the slow regime described by the shape parameter μ at high supersaturation (see **Figure 1** in CPB98).

CPB98 [45] fitted two CCN activation spectra respectively for “representative” maritime (CCN1, Type 1) and for continental (CCN2, Type 2) aerosol which are available in the standard MY05 parameterization in WRF, but the formula in Eq. (1) and corresponding fitting parameters for each aerosol type are not directly employed

for computing N_{CCN} in the microphysics scheme. Instead, maximum supersaturation is first expressed as a function of updraft speed w , temperature T , and pressure p using an iterative method outlined by [46]. To reduce computational costs, non-linear least-square fits are applied subsequently to $s_{v,w_{max}} = f(w, T, p)$ and $N_{CCN} = f(w, T, p)$ for the specified CCN spectra. For the present study, two additional CCN spectra derived from ground-based observations at Dhulikhel [26, 37] in the Kathmandu valley during JAMEX09 were incorporated into MY05 using non-linear regression fits as described in [38, 41]: (1) CCN3 (May 15, 2009) corresponding to conditions during a large-scale haze event in the Indo-Gangetic Plains (IGP) with aerosol run-up in the Central Himalayas as described by [25], thus remote aerosol; and, (2) CCN4 (May 16, 2009) corresponding to locally produced aerosols after washout of remote aerosol by rainfall in the previous day, thus local aerosol.

The CCN spectra collected before the rainfall (CCN3) and the day after (CCN4), are shown along with the standard continental (CCN2) and marine (CCN1) types from CPB98 [45] in **Figure 3**. Compared to the continental CCN2 type, CCN3 shows lower CCN number concentrations for supersaturation $S_c < 0.1\%$ and higher CCN number concentrations at higher supersaturation. The N_{CCN} for CCN4 is always lower than CCN3, but it approaches and even exceeds CCN2 for supersaturations $> 0.3\%$. This is attributed to high number concentrations of small aerosol particles that are activated at high supersaturation. The marine spectrum CCN1 (displayed only for contrast against the continental aerosol spectra) shows CN depletion halting activation at low values of supersaturation close to 0.1% .

Here, three WRF 3.8.1 simulations of regional weather on May 14–15 2009 are used to probe the sensitivity of microphysical and dynamical processes to the aerosol indirect effects (AIE) including: a control run (hereafter, CCN2) using the

**Figure 3.**

The marine (CCN type 1) and continental (CCN type 2) CCN spectra are based on the study by [45]. The CCN spectra for May 15 (CCN type 3) and May 16 (CCN type 4) are the estimated spectra from aerosol size distribution and chemical properties at Dulikhel in Central Nepal during JAMEX09 campaign [26, 37, 38]. CCN3 represents remote aerosol intrusion from the IGP. CCN4 represents local aerosol sources.

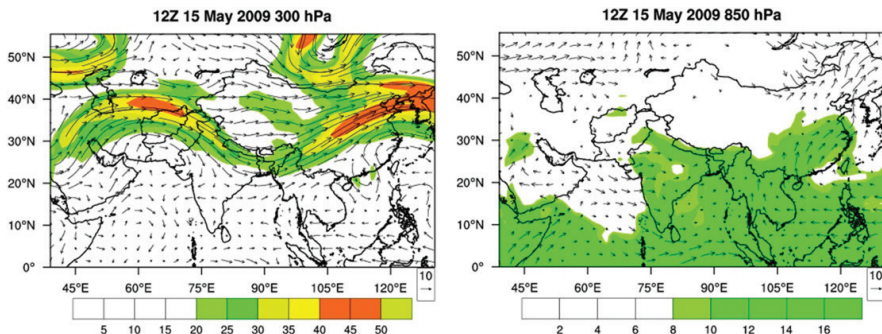


Figure 4.

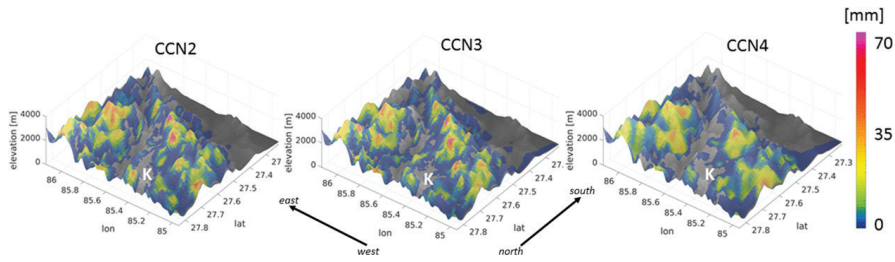
ERA interim reanalysis. Left: Wind vectors and wind speed contours at 300 hPa showing the upper level westerly jet in the free troposphere above the terrain. Right: 850 hPa wind field and mixing ratio, showing the influx of moisture to Central Nepal and the IGP where the low level flow is blocked by the terrain. <https://www.ecmwf.int/en/forecasts/datasets/archive-datasets/reanalysis-datasets>.

default continental aerosol in the MY05 microphysics scheme from CBP98, and two simulations, CCN3 and CCN4, with JAMEX09 aerosol spectra from [26, 37, 38]. The differences in model configuration among the three simulations are limited to the cloud nucleation scheme in MY05. Direct radiative effects of aerosol and the parameterization of nucleation efficiency of different ice nuclei on heterogeneous drop freezing, which could be important in ice-phase clouds [47, 48] cannot be addressed in the WRF configuration used in this study, but it is possible to examine AIE in contrasting large-scale environments, specifically during the propagation of a convective afternoon storm on May 15, second day of simulation.

The synoptic scale conditions on May 15 were characterized by northwesterly flow aloft with the axis of the upper level trough, east of the study region (**Figure 4**). The NW flow extends up to 3 km amsl. At lower levels, a cyclonic circulation is present in the IGP, creating a south-easterly flow upon the outermost foothills of the Himalayas over central Nepal. This low level flow also tends to veer along the hills westward and turn clockwise, impinging the outer ridges of Kathmandu Valley and the KWR from north-west, in agreement with the direction of upper level flow. In due course, this potentially unstable air in the lower troposphere releases its instability as it flows above the topography, triggering cells of intense precipitation. Previous studies of orographic effects on rainfall in Mesoscale Alpine Program (MAP) have also pointed out the importance of the change in static stability of the flow at low levels coupled with the orographic modification of the flow in the prediction of the intensity, location and duration of orographic precipitation [49].

3. Results and discussion

The results are analyzed with a focus on identifying and explaining differences and similarities among precipitation accumulation patterns and among microphysical vertical structure for the three different CCN activation spectra (CCN2, CCN3 and CCN4). Rain gauges operated by the Nepal Department of Hydrology and Meteorology (DHM) mostly registered zero precipitation during the 2 days of study, except in the northwest sector of d04 (**Figure 1**) were observed precipitation totals are on the order of 5–10 mm and up to 60 mm consistent with model simulations [38]. **Figure 5** shows the total precipitation accumulations for the 2nd-day of simulations draped over the 3D topography looking from the High Himalaya (north) to the IGP (south). Note the organization of rainfall hot-spots along the

**Figure 5.**

Simulated precipitation accumulation patterns on 15 May, 2009 in d04 (Figure 1) at 1 km spatial resolution. K indicates the location of Kathmandu.

ridges to the west and east of Kathmandu valley, and the much smoother patterns with more widespread low rainfall accumulations for CCN4.

Radar measurements of precipitation are non-existent in this region, and thus TRMM (Tropical Rainfall Measurement Mission) and GPM (Global Precipitation Measurement) since 2014, as well as Terra and AQUA satellite overpasses provide valuable spatial data of respectively rainfall and cloud-coverage over the region of study [7, 25, 50]. Nevertheless, the satellite trajectories vary substantially from one overpass to the next, and the observations may have therefore a limited use for storm-based case-studies depending on timing and geography. In particular, the paths of the A-Train Satellites are east and west of the innermost d04 domain on May 15, 2009. By contrast, geostationary satellites such as Meteosat7, Fengyun-2D, and Kalpana provide a regional overview of cloud processes in this region. A survey of the Meteosat7 imagery shown by [38] indicates that the storm strengthens after 0900 UTC organizing itself along the outer ridges of the Kathmandu Valley consistent with the higher precipitation accumulations on the western ridges in Figure 5. As described earlier, the north-westerly storm is fueled at low levels by south-easterly flow impinging on the southern and western ridges of the Kathmandu valley producing a series of multiple convective cores, enhanced by the complex orography (Figure 4). Consequently, the cumulative WRF rainfall shows strongly localized maxima aligned with topography, especially in the case of CCN2 and CCN3, whereas CCN4 fields are smoother with lower maxima over the western ridges, which becomes suppressed toward the foothills and the IGP.

The differences in spatial accumulation patterns (Figure 6, left panels) and cross-section (right panels) between CCN2 (dotted line) and CCN3 (red) are much smaller than the differences between CCN3 and CCN4 (blue). CCN2 and CCN3 closely follow the terrain with heavier precipitation at high elevations including isolated peaks of very high rainfall in the north and west sectors of study domain consistent with the direction of approach of the convective storm. The differences between CCN3 and CCN4 are very large to the south and west especially, with CCN4 producing higher rainfall only to the east.

Overall, the simulated rainfall patterns over the ridges surrounding Kathmandu Valley and the dry patterns in the valley itself are consistent with the patterns of observed rainfall where gauges exist. CCN2 precipitation is higher than CCN3, and both CCN2 and CCN3 are much higher than CCN4. The spatial patterns of [CCN2-CCN3] and [CCN3-CCN4] in Figure 6 exhibit the same overall spatial patterns of negative and positive differences distributed over the same sub-regions. Interestingly, both CCN2 and CCN3, yield lower rainfall amounts over the KWR and the IDR catchments. Whereas it is not possible to extrapolate based on one single storm, this result illustrates how the two CCN cases representative of remote aerosol intrusion would produce lower rainfall amounts over two critical landmarks for hydropower and water supply in the region. To extract statistically

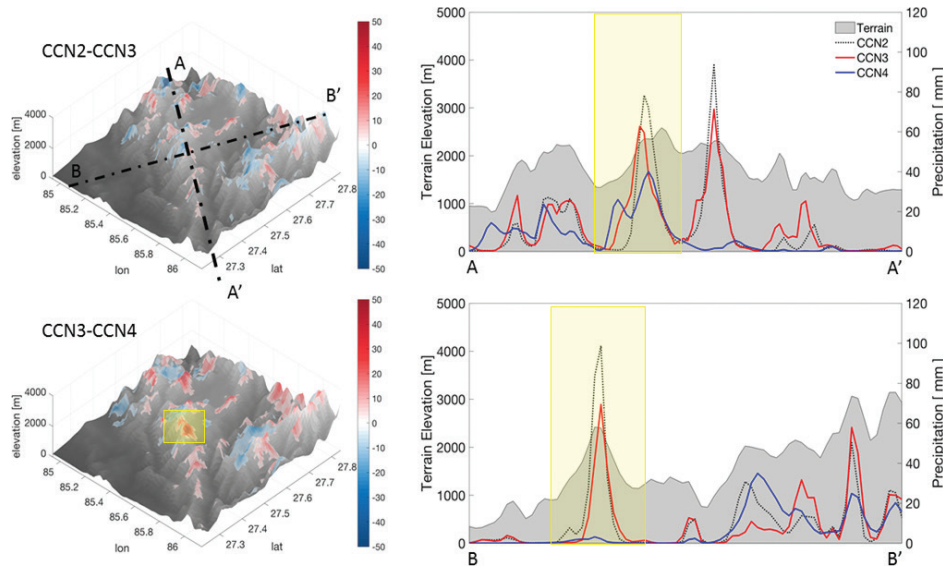


Figure 6.
 Left: Differences in spatial accumulation patterns on May 15, 2009 wrapped on the topography. Right: Cumulative rainfall along cross-sections AA' (north-south) and BB' (west-east) marked on top right panel. The topography along the cross-sections is marked in gray. The yellow box denotes the subdomain used to integrate precipitation in shown **Figure 7**.

robust information at climate time-scales, it would be necessary to produce simulations for a large number of representative storms, which is out of the scope of the present manuscript.

In the western ridges, the temporal evolution of rainfall (**Figure 7**) over the region defined by two rainfall peaks in CCN2 and CCN3 (**Figure 6**, yellow box) shows that CCN4 (local aerosol) rainfall is late compared to CCN2 and CCN3 (remote aerosol). Further, even if the second peak on the cross-section AA' (**Figure 6**, top right panel) is missed, the rainfall distribution is more filled in the case of CCN4 and when it is raining there is no significant difference in rainfall

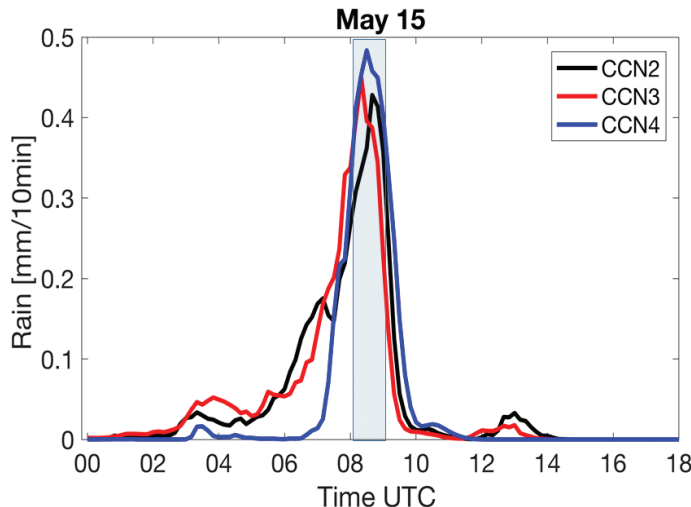


Figure 7.
 Time-series of precipitation integrated within the subdomain define by the yellow box in **Figure 6**. The light blue bar highlights the period used for hydrometeor analysis in **Figures 10 and 11**.

intensity. The delay of rainfall in CCN4 can be in part attributed to the slopes of the activation spectra shown in **Figure 3**.

Given sufficient moisture convergence at low levels, the steeper slopes of CCN2 and CCN3 lead to more rapid cloud development where orographic updrafts develop (**Figure 8**), and consequently earlier rainfall. In addition, the ACPI feedback on the intensification of individual convective cells is apparent from contrasting the strength and organization of the updrafts from 8:00 to 9:00 UTC between CCN2, CCN3 and CCN4. That is, higher rainfall accumulations at the surface are co-organized with stronger vertical updrafts and downdrafts, and thus faster hydro-meteor turn-over times. However, in the case of CCN4 the updrafts are tilted in the north-westerly direction of storm propagation (e.g., 8:20 UTC in **Figure 8**) with development of a wind gust front at low levels, which favors longer-lasting convective cells in the presence of favorable wind shear, specifically northwesterly flow aloft and southeasterly flow at low levels. The CC' cross-section at lower elevations below the ridge (AA') on the upwind slopes of the western ridges just south of KWR allows us to look at a region where CCN4 also produces higher rainfall amounts than CCN3 (**Figure 9**). The strong vertical updrafts in the green region in CCN4 correspond to convective cells forming on the steep slopes ahead of topographic peaks as low level westerly flow (**Figure 4**) from the IGP is orographically forced in the mid-Himalayas (**Figure 2**) and maintained by moist air convergence enhanced by the passage of the storm from 8:00 UTC past 9:00 UTC.

The CCN4 updrafts remain locked in space but strongly tilted with height due the strong northwesterly flow aloft (**Figure 9**, 8:20 UTC). Note the differences between CCN3 and CCN4 along CC': at high elevations, convective CCN3 cells that form in the area defined by the green bar are very short-lived (dissipate before 8:30 UTC) producing lower rainfall amounts, whereas persistent weak and shallow updraft cells locked to the topography at lower elevations in the foothills in CCN3 and in CCN4 produce little precipitation (outside of green region of interest). Interestingly, in this case the vertical structure of CCN3 and CCN4 winds is very similar indicating largely inactive moist processes, and thus no significant impact from CCN activation differences. To further examine the microphysical impacts of the three CCN types on the space-time evolution of the rainfall event, a detailed analysis of the water budget (rainwater, liquid water and ice water) is conducted next.

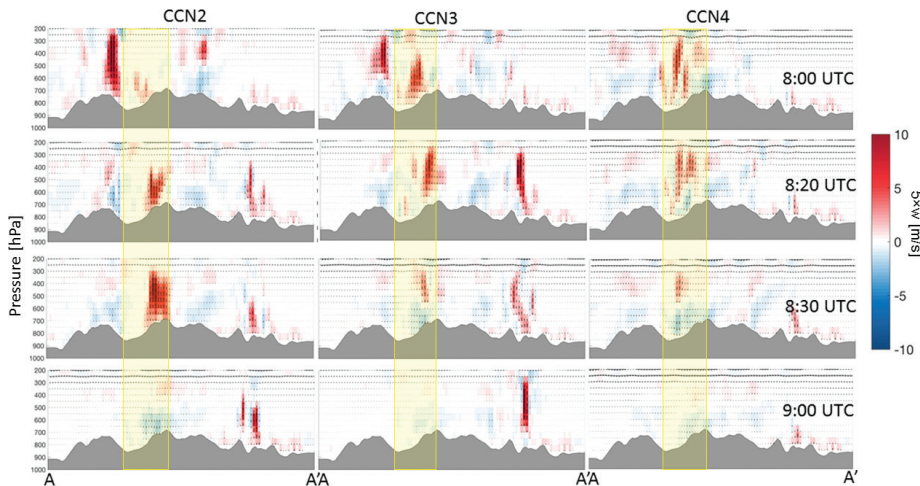


Figure 8.
Vertical distribution of westerly winds (u) and vertical winds (w) along cross-section AA' during the time of peak storm activity in **Figure 7**. As note in the legend, the vertical wind velocities were multiplied by five to stretch the scale. The yellow stripe marks approximately the location of yellow sector marked in the **Figure 6**, top right panel.

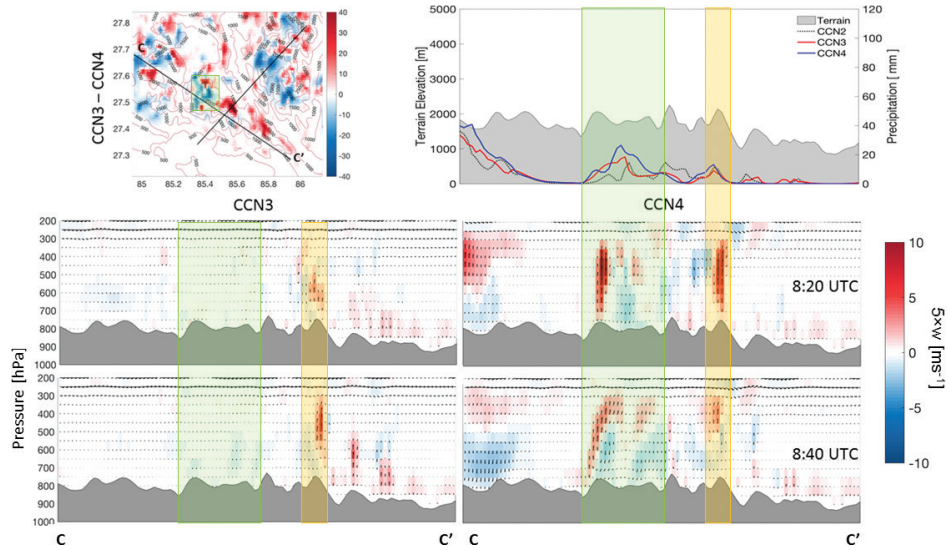


Figure 9.

Top left: Difference between CCN₃ and CCN₄ cumulative rainfall on May 15, 2009. Cross-section CC' is downslope of the ridge (AA') on the upwind side at low levels. BB' from Figure 6 also shown for reference. The green box denotes the subdomain used for analysis. Top right: Cumulative rainfall along cross-section CC' (north-south). Bottom rows: Vertical distribution of westerly (u) and vertical (w) winds along CC'. Orange bar marks location for temporal analysis in Figure 13.

Figure 10 shows the instantaneous spatial fields of Liquid Water Path (LWP, bottom row) and Ice Water Path (IWP, top row) for d04 at 8:30 UTC. Whereas some temporal and spatial variability is expected, note the consistently larger values of IWP from left to right which are representative of the overall behavior for each simulation. The cells of heavy surface rainfall, high LWP and high IWP are spatially coupled to the strong updrafts in CCN2 and CCN3. However, in the case of CCN4, even at 8:30 UTC which is the time of peak rainfall (Figure 7) in the subregion of interest, there is a gap between the position of LWP maxima (along CC') and the IWP maxima (along AA'). This is consistent with orographic warm rain processes tied to strong orographic updrafts tilted with height upstream of the ridgeline AA' (not shown), whereas at higher elevations, cold microphysics become dominant.

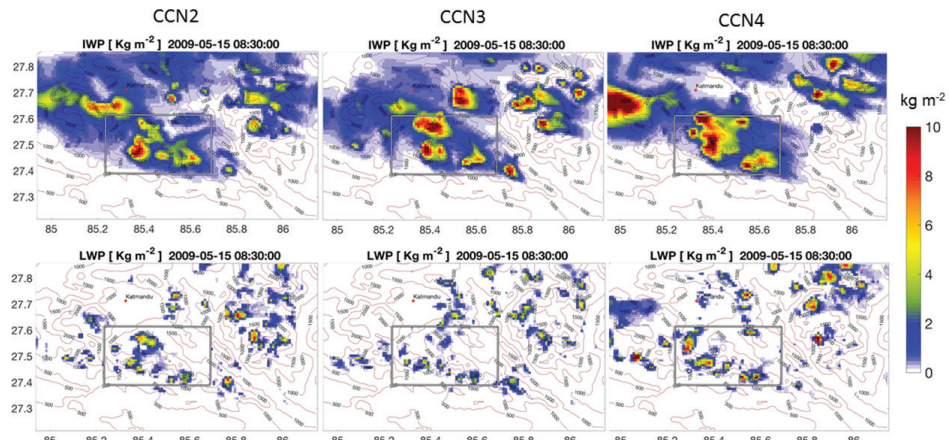


Figure 10.

Ice water path (IWP, top row) and liquid water path (LWP, bottom row) at 8:30 UTC. The gray box delimits the area used for analysis of the vertical distribution of hydrometeors in Figure 10.

The horizontal extent of the anvil of deep clouds is expected to be larger in the presence of an upper level jet [51], and this was also the case in this simulation as the strong upper level northwesterly winds aligns the anvils of the clouds along AA" in **Figure 10**. The different spatial extent of the anvils of the convective cells also influences radiative forcing (aerosol direct effect), and consequently the energy budget in the atmosphere and at the surface further complicating aerosol-cloud interactions, but this is not examined in this study.

Previous studies have shown that when there are significant increases in aerosol concentration and high numbers of cloud droplets, the efficiency of the conversion of cloud droplets to rainfall decreases along with increasing evaporative cooling of cloud droplets, resulting in increased intensity of downdrafts, cold pools, and gust fronts [13, 35]. Increased evaporative cooling due to large numbers of small droplets also affects the glaciation of shallow clouds (cloud top <5 km) by reducing autoconversion rates and secondary ice crystal production [52]. Smaller and weaker cold pools provide less forcing to the formation of secondary convection, decreasing the overall intensity and spatial reach of the convective storm. [19] found that simulated polluted storms with higher aerosol concentrations produced smaller and weaker cold pools, where the polluted aerosols were defined in terms of higher aerosol concentration. Further, [53] showed that in the absence of graupel in the representation of ice processes in the model microphysics scheme, low level downdrafts are weakened, and the simulated storm moves slower, with more rain and ice converted to snow. Snow can be transported longer distances due to their low density, leading to opposite sign impacts on precipitation due to changes in CCN concentration for simulations with and without graupel.

The spatial and temporal averages of the vertical distribution of hydrometeors for each simulation between 8:00 and 9:00 UTC are shown in **Figure 11**. The number concentrations of the various hydrometeors are not significantly different except for the cloud droplet numbers that are one order of magnitude larger in CCN4. CCN4 mixing ratios are higher for all hydrometeors. Hail forms with very

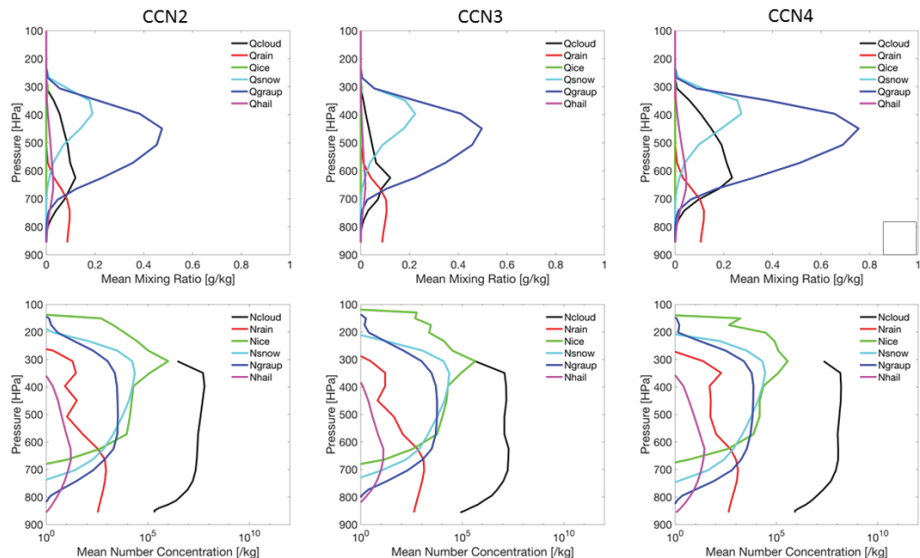


Figure 11.
Mean vertical distribution of hydrometeors within the domain defined by gray box in **Figure 9** between 8:00 and 9:00 UTC on May 15, 2009. Top row: Mean mixing ratio of mixing ratio (top row) and mean number concentration (bottom row). QXXX- mixing ratio, where XXXX: Cloud liquid water; rainfall; cloud ice; snow; graupel; and hail. NXXX- number concentration.

low concentrations and mixing ratios (pink lines) above 700 hPa, the cloud mixing ratios are high well above the freezing level especially for CCN4, thus facilitating interaction of supercooled cloud droplets with cloud ice to form snow aloft, and riming of snow hydrometeors to form graupel between 650 and 400 hPa. This is also apparent by inspecting the changes of the vertical mean number concentration of raindrops and hail on the one hand, and the decreases in the numbers of snow, whereas the mean number concentration of graupel and cloud droplets changes in parallel down to 600 hPa. The graupel mixing ratio decreases at lower levels as it settles fast and eventually melts adding to rainfall below 700 hPa. Because of the flow separation in CCN4 with weak downdrafts at low levels and weak updrafts at high levels over the ridge, the residence times of hydrometeors above 550 hPa are much longer for CCN4 which explains the higher mixing ratios of CCN4 clouds, the much higher mixing ratio of graupel, and hence the large anvils captured by the IWP fields in **Figure 10** (top right panel).

Microphysics budgets and tracking of dynamical feedbacks can be more easily carried out in simulations of isolated storm events [54] or under idealized and controlled conditions [33]. The present study consists of a succession of multiple cells and airflow over complex topography, and thus the approach is to conduct the analysis over selected subdomains within d04. Moreover, the sensitivity analysis is strictly focused on the differences in aerosol activation behavior, not on number concentration. The number of activated CCN2 will be higher than CCN3, and CCN3 will be higher than CCN4 as long as the maximum supersaturation is below 0.3% (**Figure 3**). That is, aerosol activation rates are slower for local aerosol (CCN4) than remote aerosol (CCN3) over a significant range of supersaturation values critical for cloud development, and therefore the initial numbers of hydrometeors are lower for CCN4, which delays precipitation (e.g., **Figure 7**) and forces secondary convection that is enhanced by orographic forcing on the upwind slopes (**Figure 9**) to maintain long-lived strong updrafts that produce deeper clouds with higher mixing ratios (**Figures 10** and **11**).

Although it would be expected that the horizontal advection of snow hydrometeors (low density) aloft should be important due to the presence of strong upper level northwesterly winds, the averaged vertical profiles simulations show a deep system (cloud tops >10 km) in which the dominant ice hydrometer is graupel with peak mixing ratios of 0.45 g/kg for CCN2 and CCN3 and 0.65 g/Kg for CCN4 averaged over the subdomain marked in **Figure 10** and over one-hour period (**Figure 11**). At specific times and locations, the average peak values are as high as 1.5 g/kg for CCN4 vis-a-vis 0.5 g/kg for CCN3 as shown in **Figure 12**.

Ref. [54] reported similar mean vertical profiles for cloud ice and snow in the IOP2A case-study during the Mesoscale Alpine Programme (MAP). The convective system of IOP2A also had a vertical extent exceeding 10 km, and large

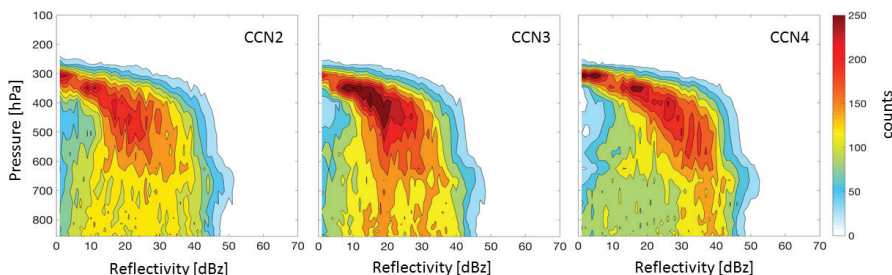


Figure 12.
*Contour frequency by altitude diagrams (CFADs) of reflectivity within the gray box domain in **Figure 10** between 8:00 and 9:00 UTC on May 15, 2009.*

amounts of graupel and hail above the freezing level albeit with much lower maximum mean mixing ratio for graupel of 0.15 g/kg and higher for hail at 0.1 g/kg. In this study, the mean hail mixing ratio is less than 0.05 g/kg. Strong and sustained uplifting of low-level moist air brings enough cloud water (with inhibited coalescence to produce rainfall, and thus high number concentrations of cloud droplets) above the freezing level to favor graupel production. This is confirmed by the significantly larger concentration of graupel in CCN4 compared to CCN2 and CCN3 (**Figures 11 and 12**). Note that the mean maximum mixing ratio of cloud water was 0.15 g/kg for IOP2A (MAP) close to the values in this study in **Figure 11** but significantly lower than instantaneous values at local places (**Figure 12**).

Figure 13 shows the Contoured Frequency Altitude Diagram (CFAD) of reflectivity for CCN2, CCN3 and CCN4 corresponding to **Figure 11** as per [55]. The probability contours are expressed in number density. The CFAD is a synthesis that overcomes the mismatch in space and time of simulated precipitation using different CCN initializations, and thus enables examining the changes in ensemble properties of the storm among different simulations. In the early stages of the storm, the distribution is broad and homogeneous at all levels (not shown here). During the mature stages of the storm, the fallout of larger hydrometeors (e.g., large raindrops and melted graupel) causes the distribution to narrow especially below the melting level (see **Figure 12**). Deep convective activity can be identified as the core region with reflectivity higher than 40 dBZ [56]. The CFAD convective core appears to be stronger with a narrow distribution in the CCN4 compared to CCN3 and CCN2, which is consistent with the budget analysis and the mean hydrometeor profiles in **Figure 11**.

It is possible that the model simulations presented here produce excessive graupel, a concern that has arisen in some studies in the past when model simulated reflectivity is compared to radar observations [57, 58]. To address these concerns, the microphysical parameterizations can be calibrated to adjust the relative proportion of graupel versus snow by for example lowering overall riming efficiency and not allowing dry growth, tuning thresholds for converting rimed snow to graupel, allowing graupel to sublime outside of the cloud reducing

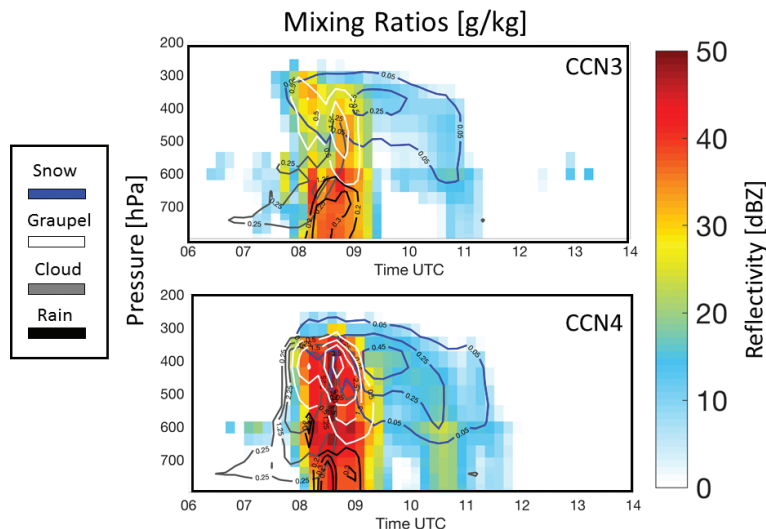


Figure 13.

Temporal evolution of the mean vertical distribution of mixing ratio for snow, graupel, cloud and rain hydrometeors and reflectivity at the location defined by the orange box in **Figure 9** on May 15, 2009. Top—CCN3; bottom—CCN4. Contour interval is 1g/kg for cloud and graupel and 0.20g/kg for snow and rain starting at 0.25g/kg for the outermost contour line.

amount of supercooled water available for riming, and by controlling the size of graupel and snow particles as a function of temperature [58]. However, the number of parameters involved is very high and the interaction of cold and warm microphysical processes with storm dynamics render this problem very difficult to address in a conclusive manner as many of the fundamental processes are not well understood yet [59–62]. The point made here is that when all else is the same, there is a significant change in precipitation patterns and 3D vertical structure depending on aerosol hygroscopicity, which is to say aerosol origin and source in the case of Central Nepal.

Analysis of the hydrometeor budgets suggests an emergent relationship between graupel production and CCN activation rate. This is illustrated by **Figure 14** that shows in the top row the vertical hydrometeor mixing ratio over the KWR for the remote aerosol (CCN3, left) and local aerosol (CCN4, right) during the time of heavier rainfall. In the bottom row, the vertical hydrometeor mixing ratio is shown for the IDR in the hour before (left panel) and during the storm (right panel) for the local aerosol. Both the KWR and the IDR areas (**Figure 2**) are on upwind slopes for the particular synoptic setup of the simulated storm: the KWR is on the southern facing slopes of the Himalayas on the upwind side with regard to westerly and southwesterly moisture advection at low levels, and the IDR is upwind with regard to the northwesterly storm propagation over the mountains. The figure shows that higher precipitation is associated with CCN4, and that the mixing ratio of graupel doubles when precipitation is heavier, and this behavior is robust across the region.

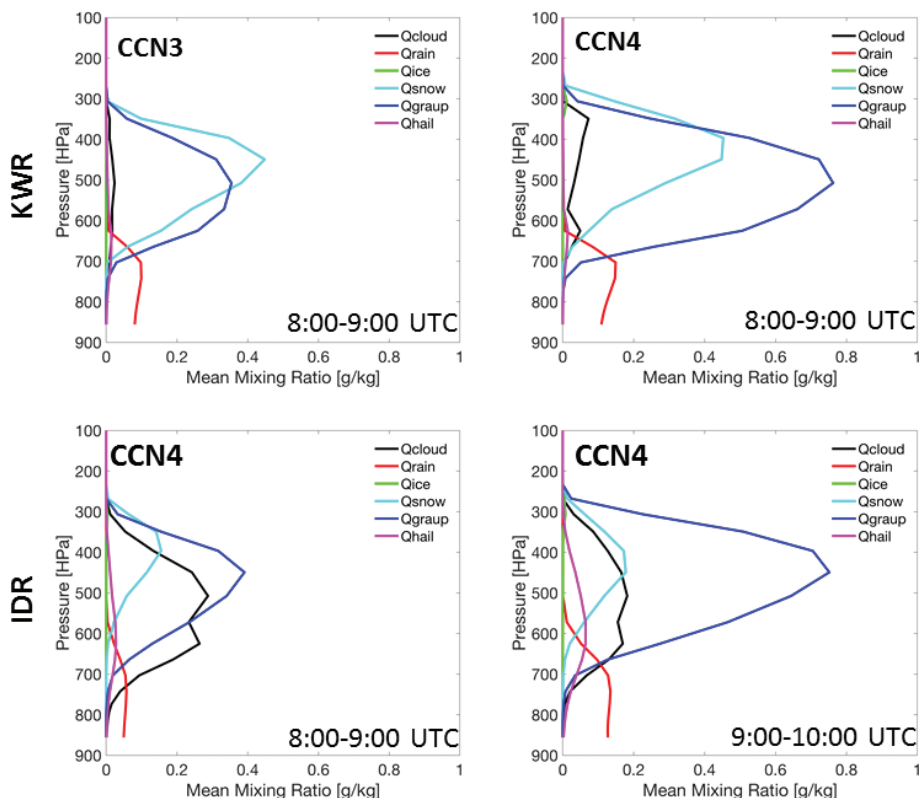


Figure 14.
*Mean vertical distribution of hydrometeor mixing ratio within the KWR (top, 8:00–9:00 UTC) and the IDR (bottom left, 8:00–9:00 UTC; bottom right, 09:00–10:00 UTC) as delineated in **Figure 2**.*

4. Summary and conclusions

A sensitivity study to examine the impact of CCN hygroscopicity on aerosol-cloud-precipitation interactions (ACPI) was conducted for a premonsoon storm in Central Nepal on May 15, 2009 during a major pollution event in the IGP using the WRF model as described in Section 2. CCN spectra used in this study included estimates from the in-situ measured aerosol size distribution and bulk hygroscopicity during JAMEX09 in Central Nepal [26, 37, 38]. Three distinct types of CCN activation spectra were used: the standard continental spectrum available in WRF, the CCN spectrum measured during the run-up of IGP pollution to the Kathmandu valley, here referred to as remote aerosol, and the CCN spectrum measured after the rainfall event when the remote aerosol was washed out and mostly aerosol from local sources is replenished in the atmosphere, here referred to as local aerosol.

An iterative method to estimate maximum supersaturation based on [46] was integrated to the double moment microphysics of MY05 [41] and implemented in WRF 8.3.1. The estimation of the maximum supersaturation in the code allows for a sensitivity study with CCN spectra fitted to the modified power law scheme of [45]. The results show that the differences in cumulative precipitation patterns between the standard and remote aerosols are small within 20%, but the differences between the simulations with remote and local aerosols are on the order of 25–50% and higher (**Figures 5 and 6**). Interestingly, these large differences could be mapped for two catchments critical for hydropower (KWR) and water resources (IDR) in Central Nepal with much lower precipitation produced with the remote aerosol than with the local aerosol. The structure and spatial extent of the vertical wind component was observed to change among the simulations due to both microphysical and dynamic forcing, with topographic forcing playing an important role in the spatial organization of long-lived updrafts on upwind slopes at mid and high elevations.

Analysis of the space-time organization of precipitation, vertical winds and microphysics suggests that sustained graupel production is favored in long-lived updrafts (enhanced and maintained by terrain induced lifting and secondary convection) for slower CCN activation spectra (i.e., local aerosol). Higher graupel mixing ratios result in heavy localized rainfall. Because of role of the terrain in locking the spatial organization of vertical velocities depending on synoptic forcing, changes in CCN type as described by its activation spectra strongly impact the spatial patterns of rainfall accumulation at the ground.

This study illustrates the importance of specifying region-based CCN for modeling studies of aerosol-cloud-rainfall interactions and provides a first indication of the range of the uncertainty in the spatial variability of precipitation that can be attributed to aerosol sensitivity in the region. Nevertheless, detailed results from this simulation are specific for the specific storm, and in order to acquire a comprehensive understanding of regional aerosol-cloud-rainfall interactions, and the impact of IGP aerosol on rainfall in the Central Himalayas, more case studies need to be analyzed of climatologically relevant storm regimes and associated aerosol.

Acknowledgements

This research was supported by the Pratt School of Engineering.

Conflict of interest

The authors declare no conflict of interest.

Author details

Ana P. Barros*, Prabhakar Shrestha, Steven Chavez and Yajuan Duan
Duke University, Durham, North Carolina, USA

*Address all correspondence to: barros@duke.edu

IntechOpen

© 2018 The Author(s). Licensee IntechOpen. This chapter is distributed under the terms of the Creative Commons Attribution License (<http://creativecommons.org/licenses/by/3.0>), which permits unrestricted use, distribution, and reproduction in any medium, provided the original work is properly cited. 

References

- [1] Barros AP. Orographic precipitation, freshwater resources, and climate vulnerabilities in mountainous regions. In: Climate Vulnerability: Understanding and Addressing Threats to Essential Resources. Vol. 5, Chapter 4. Elsevier: Elsevier Inc., 2013. pp. 57-78. DOI: 10.1016/B978-0-12-384703-4.00504-9
- [2] Wilson AM, Barros AP. Landform controls on low level moisture convergence and the diurnal cycle of warm season orographic rainfall in the southern Appalachians. *Journal of Hydrology*. 2015;531(2):475-493. DOI: 10.1016/j.jhydrol.2015.10.068
- [3] Wilson AM, Barros AP. Orographic land-atmosphere interactions and the diurnal cycle of low level clouds and fog. *Journal of Hydrometeorology*. 2017;18:1513-1533. DOI: 10.1175/JHM-D-16-0186.1
- [4] Bollasina M, Nigam S. Absorbing aerosols and summer monsoon evolution over South Asia: An observational portrayal. *Journal of Climate*. 2008;21:3221-3239. DOI: 10.1175/2007JCLI2094.1
- [5] Gautam R, Hsu NC, Lau KM, Tsay S-C, Kafatos M. Enhanced pre-monsoon warming over the Himalayan-Gangetic region from 1979-2007. *Geophysical Research Letters*. 2009;36:L07704. DOI: 10.1029/2009GL037641
- [6] Gautam R, Hsu NC, Kafatos M, Tsay S-C. Aerosol and rainfall variability over the Indian monsoon region: Distributions, trends and coupling. *Annales de Geophysique*. 2009;27:3691-3703
- [7] Shrestha P, Barros AP. Joint spatial variability of aerosol, clouds and rainfall in the Himalayas from satellite data. *Atmospheric Chemistry and Physics*. 2010;10:8305-8317. DOI: 10.5194/acp-10-8305-2010
- [8] Lau WKM. The aerosol-monsoon climate system of Asia: A new paradigm. *Journal of Meteorological Research*. 2016;30(1):001-011. DOI: 10.1007/s13351-015-5999-1
- [9] Rosenfeld D, Lohmann U, Raga GB, O'Dowd CD, Kulmala M, Fuzzi S, Reissell A, Andreae MO. Flood or drought: How do aerosols affect precipitation? *Science*. 2008;321:1309-1313. DOI: 10.1126/science.1160606
- [10] Khain AP, Rosenfeld D, Pokrovsky A. Aerosol impact on the dynamics and microphysics of convective clouds Q. *Journal of the Royal Meteorological Society*. 2005;131:2639-2663. DOI: 10.1256/qj.04.62
- [11] Seifert A, Beheng K. A two-moment cloud microphysics parameterization for mixed-phase clouds. Part II: Maritime versus continental deep convective storms. *Meteorology and Atmospheric Physics*. 2006;92:67-88
- [12] Van den Heever SC, Carrico GG, Cotton WR, Demott PJ, Prenni AJ. Impacts of nucleating aerosol on Florida storms. Part I: Mesoscale simulations. *Journal of the Atmospheric Sciences*. 2006;63:1752-1775. DOI: 10.1175/JAS3713.1
- [13] Tao W-K, Li X, Khain A, Matsui T, Lang S, Simpson J. Role of atmospheric aerosol concentration on deep convective precipitation: Cloud-resolving model simulations. *Journal of Geophysical Research*. 2007;112:D24S18. DOI: 10.1029/2007JD008728
- [14] Lynn B, Khain A, Rosenfeld D, Woodley WL. Effects of aerosols on precipitation from orographic clouds. *Journal of Geophysical Research*. 2007;112(590):D10225. DOI: 10.1029/2006JD007537

- [15] Fan J, Zhang R, Li G, Tao W-K. Effects of aerosols and relative humidity on cumulus clouds. *Journal of Geophysical Research.* 2007;112:D14204. DOI: 10.1029/2006JD008136
- [16] Khain AP, Lynn B. Simulation of a supercell storm in clean and dirty atmosphere using weather research and forecast model with spectral bin microphysics. *Journal of Geophysical Research.* 2009;114:D19209. DOI: 10.1029/2009JD011827
- [17] Khain AP. Notes on state-of-the-art investigations of aerosol effects on precipitation: A critical review. *Environmental Research Letters.* 2009;4:015004. DOI: 10.1088/1748-9326/4/1/015004
- [18] Ntelekos AA, Smith JA, Donner L, Fast JD, Gustafson WI Jr, Chapman EG, Krajewski WF. The effects of aerosols on intense convective precipitation in the northeastern United States. *Quarterly Journal of the Royal Meteorological Society.* 2009;135:1367-1391
- [19] Storer RL, Van Den Heever SC, Stephens GL. Modeling aerosol impacts on convective storms in different environments. *Journal of the Atmospheric Sciences.* 2010;67:3904-3915
- [20] Duan Y, Petters MD, Barros AP. Understanding aerosol-cloud interactions in the development of orographic cumulus congestus during IPHEx. *Atmospheric Chemistry and Physics Discussions.* 2017. DOI: 10.5194/acp-2017-396
- [21] Duan Y, Barros AP. Understanding how low-level clouds and fog modify the diurnal cycle of orographic precipitation using *in situ* and satellite observations. *Remote Sensing.* 2017;9(9):920, 33pp. DOI: 10.3390/rs9090920
- [22] Duan Y. Mapping the Impact of Aerosol-Cloud Interactions on Cloud Formation and Warm-Season Rainfall in Mountainous Regions Using Observations and Models [Thesis]. Durham, North Carolina: Duke University; 2017
- [23] Calvetti L, Filho AJP. Ensemble Hydrometeorological forecasts using WRF hourly QPF and top model for a middle watershed. *Advances in Meteorology.* 2014;2014:12. Article ID: 484120. DOI: 10.1155/2014/484120
- [24] Radhakrishna B, Zawadzki I, Fabry F. Postprocessing model-predicted rainfall fields in the spectral domain using phase information from radar observations. *Journal of the Atmospheric Sciences.* 2013;70:1145-1159. DOI: 10.1175/JAS-D-12-0175.1
- [25] Brun J, Shrestha P, Barros AP. Mapping aerosol intrusion in Himalayan valleys using the moderate resolution imaging Spectroradiometer (MODIS) and cloud-aerosol Lidar and infrared pathfinder satellite observation (CALIPSO). *Atmospheric Environment.* 2011;45:6382-6392. DOI: 10.1016/j.atmosenv.2011.08.026
- [26] Shrestha P, Barros AP, Khlystov A. Chemical composition and aerosol size distribution of the middle mountain range in the Nepal Himalayas during the 2009 pre-monsoon season. *Atmospheric Chemistry and Physics.* 2010;10:11605-11621. DOI: 10.5194/acp-10-11605-2010
- [27] Barros AP, Chiao S, Lang T, Burbank D, Putkonen J. From weather to climate—Seasonal and interannual variability of storms and implications for erosion processes in the Himalaya. *Geological Society of America Special Papers.* 2006;398:17-38. DOI: 10.1130/2006.2398 (02)
- [28] Chiao S, Barros AP. A numerical study of the Hydrometeorological Dryline in Northwest India during the monsoon. *Journal of the Meteorological Society of Japan.* 2007;85:1-25

- [29] Barros AP, Kim G, Williams E, Nesbit SW. Probing orographic controls in the Himalayas during the monsoon using satellite imagery. *Natural Hazards and Earth System Sciences*. 2004;4:1-23. DOI: 10.5194/nhess-4-29-2004
- [30] Lang TJ, Barros AP. An investigation of the onsets of 1999 and 2000 monsoons in Central Nepal. *Monthly Weather Review*. 2002;130:1299-1316
- [31] Pinty JP, Cosma S, Cohard J-M, Ricard E, Chaboreau J-P. CCN sensitivity of a warm precipitation event over fine scale orography with an advanced microphysical scheme. *Atmospheric Research*. 2001;59-60:419-446
- [32] Saleeby SM, Cotton WR, Lowenthal D, Borys RD, Wetzel MA. Influence of cloud condensation nuclei on orographic snowfall. *Journal of Applied Meteorology and Climatology*. 2009;48:903-922. DOI: 10.1175/2008JAMC1989.1
- [33] Muhlbauer A, Lohmann U. Sensitivity studies of the role of aerosols in warm-phase orographic precipitation in different dynamical flow regimes. *Journal of the Atmospheric Sciences*. 2008;65:2522-2542. DOI: 10.1175/2007JAS2492.1
- [34] Iguchi T, Nakajimam T, Khain AP, Saito K, Takemura T, Suzuki K. Modeling the influence of aerosols on cloud microphysical properties in the East Asia region using a mesoscale model coupled with a bin-based cloud microphysics scheme. *Journal of Geophysical Research*. 2008;113:D14215. DOI: 10.1029/2007JD009774
- [35] Lee SS, Donner LJ, Penner JE. Thunderstorm and stratocumulus: How does their contrasting morphology affect their interactions with aerosols? *Atmospheric Chemistry and Physics*. 2010;10:6819-6837. DOI: 10.5194/acp-10-6819-2010
- [36] Dey S, Di Girolamo L. A climatology of aerosol optical and microphysical properties over the Indian subcontinent from 9 years (2000-2008) of multiangle imaging Spectroradiometer (MISR) data. *Journal of Geophysical Research*. 2010;115(D15):D15204. DOI: 10.1029/2009JD013395
- [37] Shrestha P, Barros AP, Khlystov A. CCN estimates from bulk hygroscopic growth factors of ambient aerosols during the pre-monsoon season over Central Nepal. *Atmospheric Environment*. 2013;67:120-129. DOI: 10.1016/j.atmosenv.2012.10.042
- [38] Shrestha P. Characterization of Pre-Monsoon Aerosol and Aerosol-Cloud-Rainfall Interactions in Central Nepal [Thesis]. Durham, North Carolina: Duke University; 2011
- [39] Skamarock WC et al. A Description of the Advanced Research WRF Version 3. Boulder CO: National Center for Atmospheric Research; 2008; Report TN-475+STR. DOI: 10.5065/D68S4MVH
- [40] Kain JS. The Kain-Fritsch convective parameterization: An update. *Journal of Applied Meteorology*. 2004;43:170-181
- [41] Milbrandt JA, Yau MK. A multimoment bulk microphysics parameterization. Part II: A proposed three-moment closure and scheme description. *Journal of the Atmospheric Sciences*. 2005;3065-3081. DOI: 10.1175/JAS3816.1
- [42] Iacono M et al. Radiative forcing by long-lived greenhouse gases: Calculations with the AER radiative transfer models. *Journal of Geophysical Research*. 2008;113:D13103. DOI: 10.1029/2008JD009944
- [43] Tewari M et al. Implementation and verification of the unified NOAH land surface model in the WRF model. In: 20th conference on weather analysis

and forecasting/16th conference on numerical weather prediction; 2004. pp. 11-15

[44] Nakanishi M, Niino H. An improved Mellor-Yamada level-3 model with condensation physics: Its design and verification. *Boundary-Layer Meteorology*. 2004;112:1-31. DOI: 10.1023/B:BOUN.0000020164.04146.98

[45] Cohard J-M, Pinty J-P, Bedos C. Extending Twomey's analytical estimate of nucleated cloud droplet concentration from CCN spectra. *Journal of the Atmospheric Sciences*. 1998;55:3348-3357

[46] Cohard J-M, Pinty J-P. A comprehensive two-moment warm microphysical bulk scheme I: Description and tests. *Quarterly Journal of the Royal Meteorological Society*. 2000;126:1815-1842. DOI: 10.1002/qj.49712656613

[47] Diehl K, Simmel M, Wurzler S. Effects of drop freezing on microphysics of an ascending cloud parcel under biomass burning conditions. *Atmospheric Environment*. 2007;41:303-314. DOI: 10.1016/j.atmosenv.2006.08.011

[48] Hoose C, Kristjansson JE, Chen J-P, Hazra A. A classical-theory-based parameterization of heterogeneous ice nucleation by mineral dust, soot, and biological particles in a global climate model. *Journal of the Atmospheric Sciences*. 2010;67:2483-2503. DOI: 10.1175/2010JAS3425.1

[49] Medina S, Houze RA Jr. Air motions and precipitation growth in alpine storms. *Quarterly Journal of the Royal Meteorological Society*. 2003;129:345-337

[50] Barros AP, Joshi M, Putkonen J, Burbank DW. A study of the 1999 monsoon rainfall in a mountainous region in Central Nepal using

TRMM products and raingauge observations. *Geophysical Research Letters*. 2000;27(22):3683-3686. DOI: 10.1029/2000GL011827

[51] Koren I, Remer LA, Altaratz O, Martins JV, Davidi A. Aerosol-induced changes of convective cloud anvils produce strong climate warming. *Atmospheric Chemistry and Physics*. 2010;10:5001-5010. DOI: 10.5194/acp-10-5001-2010

[52] Phillips VTJ, Donner LJ, Garner ST. Nucleation processes in deep convection simulated by a cloud-system-resolving model with double-moment bulk microphysics. *Journal of the Atmospheric Sciences*. 2007;64: 738-761. DOI: 10.1175/JAS3869.1

[53] Lim K-SS, Hong S-Y, Yum SS, Dudhia J, Klemp JB. Aerosol effects on the development of a supercell storm in a double-moment bulk-cloud microphysics scheme. *Journal of Geophysical Research*. 2011;116:d02204. DOI: 10.1029/2010JD014128

[54] Lascaux F, Richard E, Pinty J-P. Numerical simulation of three different MAP IOPs and the associated microphysical processes. *Quarterly Journal of the Royal Meteorological Society*. 2006;132:1907-1926. DOI: 10.1256/qj.05.197

[55] Yuter SE, Houze RA Jr. Three-dimensional kinematic and microphysical evolution of Florida cumulonimbus. Part II: Frequency distributions of vertical velocity, reflectivity, and differential reflectivity. *Monthly Weather Review*. 1995;123:1941-1963

[56] Lang S, Tao W-K, Simpson J, Ferrier B. Modeling of convective-Stratiform precipitation processes: Sensitivity to partitioning methods. *Journal of Applied Meteorology*. 2003;42:505-527

[57] Lang SE, Tao W-K, Zeng X, Li Y. Reducing the biases in simulated radar

Reflectivities from a bulk microphysics scheme tropical convective systems. Journal of the Atmospheric Sciences. 2011;68:2306-2320. DOI: 10.1175/JAS-D-10-05000.1

[58] Tao W-K et al. The impact of microphysical schemes on hurricane intensity and track. Asia-Pacific Journal of Atmospheric Sciences. 2011;47(1): 1-16. DOI: 10.1007/s13143-011-1001-z

[59] Tao W-K et al. High-resolution NU-WRF model simulations of MC3E, deep convective-precipitation systems: Comparisons between Goddard microphysics schemes and observations. Journal of Geophysical Research – Atmospheres. 2016;121:1278-1306. DOI: 10.1002/2015JD023986

[60] Fan J et al. Cloud-resolving model intercomparison of an MC3E squall line case: Part I—Convective updrafts. Journal of Geophysical Research – Atmospheres. 2017;122:9351-9378. DOI: 10.1002/2017JD026622

[61] Barnes HC, Houze R Jr. Comparison of observed and simulated spatial patterns of ice microphysical processes in tropical oceanic mesoscale convective systems. Journal of Geophysical Research-Atmospheres. 2016;121: 8269-8296. DOI: 10.1002/2016JD025074

[62] Khain AP et al. Representation of microphysical processes in cloud resolving models: Spectral (bin) microphysics versus bulk parameterization, rev. Geophysics. 2015;53:247-322. DOI: 10.1002/2014RG000468